Structural diversity in binary superlattices from Au and g-Fe 2O3 nanocrystals: towards fine tuning of dipolar interactions

Suyeon Lee, Anh-Tu Ngo, Isabelle Lisiecki, Alexa Courty

Structural diversity in binary superlattices from Au and γ-Fe_2O_3 nanocrystals: towards fine tuning of dipolar interactions

Suyeon Lee[1], Anh-Tu Ngo[1], Isabelle Lisiecki[1]* and Alexa Courty[1]*

1-Sorbonne Université, MONARIS, UMR8233, UMR 8233, F-75005 Paris, France

KEYWORDS: Binary superlattices, crystalline structure, gold and maghemite nanoparticles, superlattice growth, magnetic properties.

ABSTRACT

Two cooperative and complementary components such as γFe_2O_3/Au nanoparticles (NPs) are used to grow binary superlattices (BNSLs). The effects of different parameters including concentration ratio of colloidal solutions, effective size ratio of NPs, deposition temperature and type of solvent on the formation of BNSLs are discussed. A systematic study of the effect of these parameters is performed to determine the driving forces underlying the BNSL formation. We show that by using the same batch of particles, the control of the various parameters gives rise to a large diversity of crystalline structures. In addition, thanks to their long-range organization, the magnetic properties of γ-Fe_2O_3/Au NPs binary superlattices are studied by SQUID magnetometry and compared to those of pure γ-Fe_2O_3 NPs superlattices. The γ-Fe_2O_3 interparticle distance modulated by the insertion of Au NPs is shown to significantly impact their magnetic properties.

INTRODUCTION

The term binary superlattices (BNSLs) refers to the assemblies of nanomaterials composed of two different cooperative complementary components inducing synergistic effects[1–5] . Usually, two or more individual components are synthesized separately, then binary superlattices are fabricated by using the same methods used to fabricate the 3D assemblies composed of one type of NPs [6–9]. Spherical particles characterized by a low size polydispersity can usually self-assemble into superlattices with either face-centered cubic (*fcc*) or hexagonal close packed (*hc*) crystalline structure[6,10–12]. In addition to their multi-component characteristics, binary mixtures naturally provide a much richer class of structures. In order to co-crystallize, NPs must meet, as far as possible, the requirements of given geometrical principles. In the simplest approach, the formation of a binary assembly is expected only if its compactness exceeds that of single-component crystals in *fcc* or *hcp* (0.74)[13]. This principle of space filling is still widely used for predicting the behavior of particles in binary mixtures. Particle size ratio (R_{small}/R_{large}) and concentrations are considered as key factors determining the structure of binary assemblies [5,14,15]. Considering the geometric considerations, we can predict the formation of BNSLs structure such as AB, AB_2, or AB_{13}[4]. The interparticle distance (between NPs A) can be increased through the insertion of NPs B (with possible different sizes) in the BNSLs as compared to the single component superlattices (made of NPs A). Consequently, the strategy of binary superlattices offers a possibility to tune the dipolar interactions between the magnetic[16] or non-magnetic[17] NPs (NPs A) and thus to control the collective physical properties. Furthermore, the binary superlattices constitute ideal candidates to favor coupling between NPs of different properties (e.g., plasmonic, magnetic, dielectric or excitonic), which is expected to result in tunable and/or novel collective properties.

On one hand, understanding the interaction between both types of components in BNSLs is crucial to fabricate the appropriate and desired binary structure. On the other hand,

while the first binary superlattices have been reported in 1998, the study of their physical properties in view of possible applications is still a challenge in nanoscience[18]. While much of the literature on BNSLs has focused on their lattice structure and their formation, in a few instances their physical properties were studied[16,19–21]. Chen et al.[16] have revealed the collective dipolar interactions between magnetite (Fe_3O_4) nanoparticles of two different sizes when they are organized in binary superlattices (BNSLs). Sanchez et al.[21] have evidenced a collective behavior resulting from strongly coupled magnetic dipolar systems of NPs of maghemite (γ-Fe_2O_3) having two different sizes and mixed in different proportions. In our case, we form binary superlattices (BNSLs) with a magnetic (maghemite) and non-magnetic (gold) NPs, which gives us the possibility to use the Au nanoparticles as spacer building blocks for fine-tuning of magnetic dipolar interactions between γ-Fe_2O_3 nanoparticles.

Here, we first focus on structural study of binary assemblies made of Au and γ-Fe_2O_3 NPs. The influence of different parameters including deposition temperature (T_d), γ-Fe_2O_3/Au effective size ratio γ_{eff}, and [γ-Fe_2O_3]/[Au] concentration ratio is studied to optimize their organization. Second and thanks to their long-range organization, the magnetic properties of γ-Fe_2O_3/Au NP BNSLs are studied by SQUID magnetometry and compared to those of pure γ-Fe_2O_3 NPs superlattices.

METHODS

Products. All chemicals were used without further purification. 1-dodecanethiol (98%), hexane (99%) and ethanol absolute (99%), oleic acid (90%) and 1-octadecene (90%) were purchased from Sigma-Aldrich. Tertbutylamine borane complex (97%) is from STREM Chemicals. Toluene (99%) and dodecanoic acid (99.5%) were bought from ACROS Organics. Gold(I) chloride triphenylphosphine ($ClAu(PPh_3)$) was purchased from STREM. Iron chloride

($FeCl_3.6H_2O$, 99%) was purchased from Prolabo. Sodium dodecanoate ($CH_3(CH_2)_{10}COONa$) and sodium oleate ($C_{18}H_{33}NaO_2$), (97%) was purchased from TCI.

Transmission Electron Microscopy (TEM). TEM study was performed using a JEOL JEM-1011 microscope at 100 kV. The diameters are measured from at least 500 NPs deposited on a TEM grid coated with amorphous carbon. The effective diameters ($D_{c\text{-}c}$) were obtained from several line profiles performed on the TEM images via Image J 1.52a.

Magnetic measurements. Magnetic measurements were carried out on a commercial SQUID magnetometer (Cryogenic S600) with a field of 20 Oe for the zero-field cooled (ZFC)/field cooled (FC) susceptibility curves, and with fields up to 5 T for the magnetization curves. All magnetic measurements were carried out on thin BNSLs (4 or 5 layers) deposited on TEM grids and previously characterized by TEM. During the measurement, the applied field is parallel to the substrate. For the ZFC measurement, the sample was cooled from 300 K to 3 K with no field and then heated to 300 K in a field of 20 Oe to record the magnetization $M_{ZFC}(T)$ of the sample. Then, for the FC measurement, the sample is cooled again to 3K under ~~20 Oe~~ the same applied field and the magnetization M_{FC} (T) was recorded. In both cases, the measurements were performed on heating with, for each temperature step, a heating rate of the order of 1 $Kmin^{-1}$. The measurement time was about 1 s. Hysteresis curves were performed at 3 K.

Synthesis of Au nanocrystals. Au NPs were synthesized through a revisited method from the Stucky group [22,23]. 0.25 mmol of gold(I) chlorodiphenylphosphine ($AuClPPh_3$) complex was dissolved in 25 mL of toluene with 500 µL of 1-dodecanethiol (C_{12}). The gold precursor is reduced by adding a solution of tert-butylamine borane (TBAB) complex (2.5 mmol dissolved

in 5 mL of toluene). The reaction took place at 100°C under vigorous stirring for 5 min. The formation of Au NPs was evidenced by the color change of the solution from colorless to dark red. After the reaction, a washing step is necessary to remove all by-products. First, all the solvent was evaporated, and the same amount of ethanol was added, then the solution was centrifuged. The precipitate was then dispersed in organic solvent such as toluene. The resulting dodecanethiol- coated NPs were characterized by a mean diameter of 4.6 nm with a size distribution of 7% (Figure S1, Supporting Information).

Synthesis of γ-Fe_2O_3 nanocrystals. The maghemite (γ-Fe_20_3) NPs with 12.4 nm (σ=8%), 11.4 nm, (σ=8%) and 7.9 nm (σ=8%) were synthesized using modified procedure from Park et al and developed few years ago in MONARIS [24,25] (Figure S2, Supporting Information). For the 12.4 nm diameter maghemite NPs, the reactants sodium oleate and oleic acid (C_{18}) are replaced by sodium laurate and lauric acid (C_{12}). The typical synthesis of the iron–laurate complex is performed by mixing iron chloride ($FeCl_36H_2O$) and sodium laurate in a solvent mixture composed of ethanol, distilled water, and hexane. The mixture is refluxed at 66 °C for 4 h and the organic phase is washed three times with ultrapure water in a separatory funnel. The remaining hexane in the organic phase is evaporated under vacuum in a rotavapor at 32 °C. The iron–laurate complex is then washed three times with a mixture of ethanol and hexane and evaporated at 40 °C. In a typical synthesis of maghemite nanocrystals, 1.05 g of the iron–laurate complex is dissolved in a mixture of 10 ml of 1-octadecene and 0.64 g of lauric acid at room temperature. This mixture is heated to the boiling point of 1-octadecene (b.p: 317 °C) under vigorous stirring and is refluxed for 30 min and then cooled to room temperature. A black gel containing the nanocrystals is formed. The nanocrystals are separated and washed with a large excess of hexane, ethanol, and acetone.

For the 11.4 nm and 7.9 nm maghemite NPs, we replaced the sodium laurate and lauric acid by sodium oleate and oleic acid. The procedures for synthesizing the reactant (iron oleate complex) and particles are similar as those described above. The 7.9 nm diameter maghemite NPs were synthesized using 1.42 g of iron–oleate complex dissolved in a mixture of 10 mL of 1-octadecene and 0.9 g of oleic acid. By heating this mixture for 2h at 100°C to remove water residues before heating up to the boiling point of 1-octadecene under vigorous stirring and keeping under refluxed for 30 min, 11.4 nm maghemite NPs are obtained. The NPs are then dispersed in organic solvent such as chloroform or toluene.

Supercrystal growth of BNSLs of γ-Fe_2O_3 and Au NPs. Two deposition methods were used (Figure S3, Supporting Information): i) The *immersion method* [26]. The BNSLs growth was performed through the slow evaporation of binary colloidal solutions[8,26,27]. The samples were prepared by horizontally immersing an amorphous carbon coated TEM grid in 20 µL of a mixed colloidal solution, in a glass vial. The glass vial was itself placed in a temperature-controlled chamber, under a nitrogen flow. The temperature was controlled by water circulation. Different parameters were controlled: the γ-Fe_2O_3/Au effective size ratio γ_{eff} (0.45; 0.48; 0.64), the [γ-Fe_2O_3]/[Au] concentration ratio (1/1; 1/4; 1/7), the type of solvent (hexane, toluene or cumene) and the substrate temperature, Td, (35°C; 50°C; 65°C). ii) The *liquid-liquid interface deposition method*[28,29]. This method is based on the use of a bad solvent, ethylene glycol (EG) in our case. It is called a bad solvent because it cannot solubilize the alkyl chain coated NPs, which then agglomerate at its top. A Teflon beaker, placed in a temperature-controlled chamber, under a nitrogen flow, was filled with EG. On the EG top, 20 µl of the mixed colloidal solution was then deposited. The resulting NPs film was collected and deposited on an amorphous TEM grid with a filter paper underneath to absorb EG solvent in excess. The depositions were performed

with γ-Fe_2O_3/Au effective size ratio γ_{eff} equal to 0.64 and [γ-Fe_2O_3]/[Au] concentration ratio equal to 1/1 and 1/4. The solvent was toluene and the substrate temperature, Td, was 50°C.

Supercrystal growth of superlattices of γ-Fe_2O_3 NPs: The SLs growth was performed through the immersion method. Maghemite NPs colloidal solution dispersed in toluene were slowly evaporated on amorphous carbon coated TEM grid in glass vial (Figure S3, Supporting Information). The volume of colloidal solution was fixed with 20 µl. This glass vial was placed in temperature-controlled chamber under nitrogen flow. The temperature was controlled at 50°C during whole evaporation.

RESULTS AND DISCUSSION

1- Formation of binary superlattices of Au and γ-Fe_2O_3 NPs

The NPs A and B used as building blocks to form binary superlattices have to meet stringent requirements: i) a narrow size distribution (≤10 %), a prerequisite to favor long-range self-organization, ii) if appropriate as this is the case in our study, a given effective NP size ratio (around 0.5) between smaller and larger components[30,31] and iii) suitable combination ligand/solvent which allow optimal interactions between NPs to first avoid the aggregation between NPs, second, to favor the formation of BNSLs and third, to prevent the NP segregation[17,31].

In order to deeper understand and then, well master the formation of BNSLs, we have investigated, in the following part, the influence of a full set of parameters (effective NP size ratio, type of ligand, type of solvent, deposition temperature and deposition process). Thanks

to their low size distribution and their magnetic and plasmonic property respectively, γ-Fe_2O_3 and Au NPs are chosen as the two components.

1.1- Effect of the effective NP size ratio and ligand type

The formation of BNSLs is first studied by varying the following key parameters: the effective NP size ratio (γ_{eff}= $D_{C\text{-}C}$ (Au))/$D_{C\text{-}C}$ (γ-Fe_2O_3)) and the type of NP ligand. The effective NP diameter ($D_{C\text{-}C}$) is defined as the center-to-center distance between gold or maghemite NPs when they are organized in 3D hexagonal network and is calculated from line profiles performed on TEM image (Figure S1 and S2). $D_{c\text{-}c}$ value takes thus into account the soft ligand corona and the metal core diameter [5]. The effective length for C_{12} and C_{18} type ligands deduced from the difference between $D_{C\text{-}C}$ and the diameter D (see Table 1) for close packed assembly of maghemite or a gold NPs are respectively found equal to 2 and 1.8 nm respectively. These values are consistent with those obtained with similar metal nanoparticles having the same coating agent [6,32]. These reduced effective lengths were ascribed to interdigitation of the alkyl chains. Three different diameters D of γ-Fe_2O_3 NPs (12.4, 11.4, and 7.9 nm) coated with oleic acid (C_{18}) or lauric acid (C_{12}) are considered, keeping a single size of Au NPs (4.6 nm), coated with dodecanethiol (C_{12}). The corresponding effective diameter of both components and effective size ratio of the three combinations of NPs are given in Table 1. The colloidal solvent used for both components is toluene and the concentration ratio ([γ-Fe_2O_3]: [Au]) is equal to 1/4. The growth of BNSLs is performed by using the immersion method, at controlled deposition temperature, 50 °C (Table 2).

Table 1. Summary of the γ-Fe_2O_3 and Au NPs differing by their diameters, nature of ligands (with C_n carbon atoms), effective diameters (D) and effective size ratio (γ_{eff}) in the corresponding binary superlattices (BNSLs)

NP type	**ligands**	**Diameter *D* (nm)**	**Effective diameter D_{C-C} (nm)**	**γ-Fe_2O_3/*Au* BNSLs/ effective size ratio (γ_{eff})**
γ-Fe_2O_3	Lauric acid (C_{12})	12.4	14.2	0.45
	Oleic acid (C_{18})	11.4	13.4	0.48
	Oleic acid (C_{18})	7.9	10	0.64
Au	*Dodecanethiol (C_{12})*	*4.6*	*6.4*	

Table 2. Growth conditions of BNSLs.

Fixed parameter	**Condition**
Concentration ratio ([γ-Fe_2O_3]:[Au])	1:4 (0.1 wt.% : 0.4 wt. %)
Solvent	Toluene
Volume of NPs	40 (µl)
deposition method	Immersion method
Deposition temperature (T_d)	50 °C

TEM study reveals those three different structural types of BNSLs: NaCl (Space Group Fm3m), AlB_2 (Space Group P6/mmm), $NaZn_{13}$ (Space Group Fm3c), which are obtained by varying the effective nanoparticle size ratio γ_{eff} (0.45; 0.48 and 0.64), keeping the other conditions unchanged (T_d and [γ-Fe_2O_3]/[Au]) (Figure 1). The TEM image in Figure 1a show typical (111) crystal planes of NaCl-type binary superlattices with the corresponding model in the insets for an effective size ratio γ_{eff}=0.45. The size of the crystal domains of the NaCl-type binary structure is several micrometers (see low magnification TEM images in Figure S4a, Supporting Information). A further increase of γ_{eff} to 0.48 and 0.64 gives rise to AlB_2 and $NaZn_{13}$ type binary structures respectively (Figure 2b and c). The corresponding model are in insets. The size of the crystal domains of both binary structures can reach 1-2 µm (Figures S4b and c, Supporting Information). For AlB_2-type structure, the crystal has the (110) plane parallel to the substrate (Figure 1b). For $NaZn_{13}$-type structure, the TEM image represents the icosahedral $NaZn_{13}$ from the preferential crystal orientation with the (100) plane parallel to the substrate (Figure 1c).

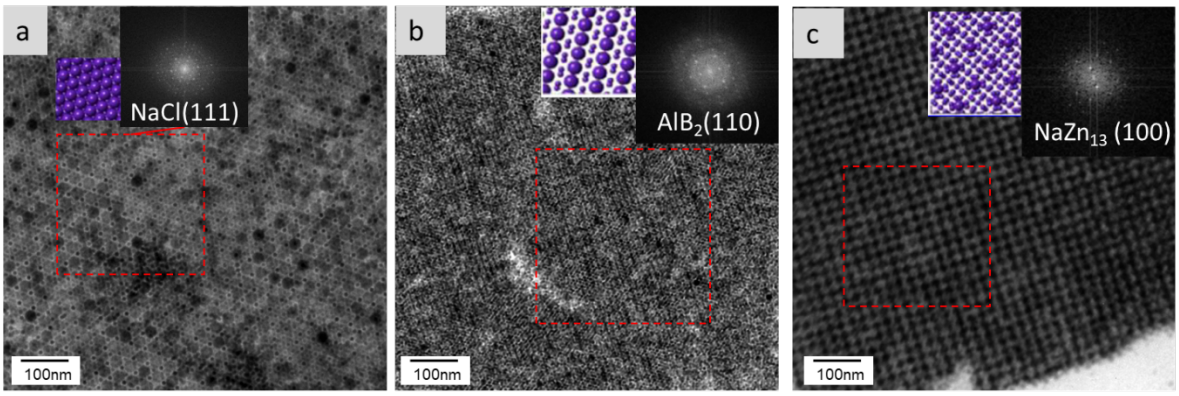

Figure 1. TEM images of binary superlattices composed of γ-Fe_2O_3 and Au NPs, with different effective size ratio (γ_{eff}), keeping the other conditions unchanged ([γ-Fe_2O_3]/[Au])=1/4, T_d=50°C), γ_{eff} = (a) 0.45 (b) 0.48 (c) 0.64. Insets (right) show selected area FFT analysis. Insets (left) show BNSL structure corresponding to TEM images.

At lower magnification (Figure S4, Supporting Information), TEM study reveals the presence of cracks, which tends to indicate a layer-by-layer growth for these NaCl, AlB_2, $NaZn_{13}$-type superlattices [12].

These results show that tunable type-structure BNSLs combining Au NPs (4.6 nm) and γ-Fe_2O_3 NPs can be obtained with various effective size ratio, γeff, ($0.45 \leq 0.48 < 0.64$), that is, at various γ-Fe_2O_3 effective diameter (14.2 nm > 13.4 nm > 10 nm). The increase in the effective size ratio favors a transition of BNSL type-structure from NaCl towards AlB_2 and finally towards $NaZn_{13}$ structures. The BNSLs structures observed in this study are in accordance with the phase diagram for binary hard spheres mixtures[5,13,33,34]. This is well illustrated on the Table 3, which compares the various structures of binary superlattices obtained for the different nanoparticle effective size ratio values, at the atomic scale (theoretical) and the NP scale (our experimental study). This confirms that at given temperature (50 °C) and concentration ratio ([γ-Fe_2O_3]/[Au] =1/4), the hard-sphere model designed for atoms can, to some extent, be used for NPs. Consequently, we show that the binary superlattices can be simply predicted from the spacing filling curves.

Table 3. Comparison of BNSL structures that are experimentally obtained with those predicted by the phase diagrams for binary hard spheres mixtures[5,34]for various effective size ratio values.

	NaCl	AlB_2	$NaZn_{13}$
Ref. [34]	$0.421 \leq \gamma_{eff} \leq 0.45$	$0.45 \leq \gamma_{eff} \leq 0.54$	$0.54 \leq \gamma_{eff} \leq 0.65$
$D_{C\text{-}C}$(Au) /$D_{C\text{-}C}$(γ-Fe_2O_3)	$\gamma_{eff} = 0.45$	$\gamma_{eff} = 0.48$	$\gamma_{eff} = 0.64$

1.2. Effect of the [γ-Fe_2O_3]/[Au] concentration ratio and deposition temperature (Td)

The effective size ratio is not the single key parameter to impact the BNSLs structure. Previous studies have shown that a change in the concentration ratio of colloidal solutions can induce a phase transformation in binary NP SLs[15,35]. In light of this, we studied the influence of [γ-Fe_2O_3]/[Au] concentration ratio combined to the deposition temperature (T_d) with our system. We focus on the combination oleic acid coated γ-Fe_2O_3 NPs (7.9 nm) and dodecanethiol coated Au NPs (4.6 nm) NPs, leading to an effective size ratio γ_{eff} equal to 0.64 (Table1). The colloidal solvent is toluene. TEM images in Figure 2 show that BNSL type-structure significantly depends on both the [γ-Fe_2O_3]/[Au] concentration ratio and the deposition temperature (Td). First, at T_d=50 °C, the decrease in the concentration ratio from 1/1 to 1/4 or 1/7 induces the structural transition of BNSL type-structure from CuAu to $NaZn_{13}$. A similar behavior is observed at Td=65°C. At Td=35 °C, CuAu-type structure is observed for concentration ratios [γ-Fe_2O_3]/[Au]=1/1 and 1/4. At low concentration ratio [γ-Fe_2O_3]/[Au]=1/7, $NaZn_{13}$-type with high density of Au NPs remains dominant. At the intermediate ratio [γ-Fe_2O_3]/[Au]=1/4, amorphous arrangements are also observed (Figure 2d).

On one hand, the deposition temperature influences the solvent evaporation rate of the colloidal mixture and then the formation of superlattices. On the other hand, the formation of superlattices in line with the theoretical phase diagrams of binary hard-sphere mixtures typically requires relatively high temperatures[33]. However, exceeding boiling point of solvent prevents the NP organization. Our results clearly show that, for γ_{eff} value equal to 0.64, the well-known hard sphere model of atomic binary bulk material is valid for NPs in a rather restrictive domain related to the relative concentration of large to small nanoparticles and depends on the deposition temperature (T_d). This is valid with 1/4 ≤ [γ-Fe_2O_3]/[Au] ≤1/7 for a substrate temperature T_d ≥50°C and with [γ-Fe_2O_3]/[Au] =1/7 for a substrate temperature

T_d=35°C. Nevertheless, the AuCu type structure considered as unstable for γ_{eff}=0.64 according to the hard sphere model is produced with [γ-Fe_2O_3]/[Au]=1/1 for values of Td from 35°C to 65°C and with [γ-Fe_2O_3]/[Au]=1/4 for Td=35°C. This study clearly shows that the relative concentration of γ-Fe_2O_3 and Au nanoparticles as well as the substrate temperature, are powerful tools to control the BNSL structure, in addition to the space filling (entropic) principle. Furthermore, these results show that BNSL structures with the same stoichiometry can be produced in several polymorphic forms, here NaCl and CuAu, by adapting the particle size and deposition conditions (deposition temperature and concentrations ration). They are in good agreement with previous results obtained by Shevchenko et al. [4] Table 4 summarizes the different BNSL structures depending on the particle size and deposition conditions (concentration ratio of colloidal solutions, effective size ratios and deposition temperature).

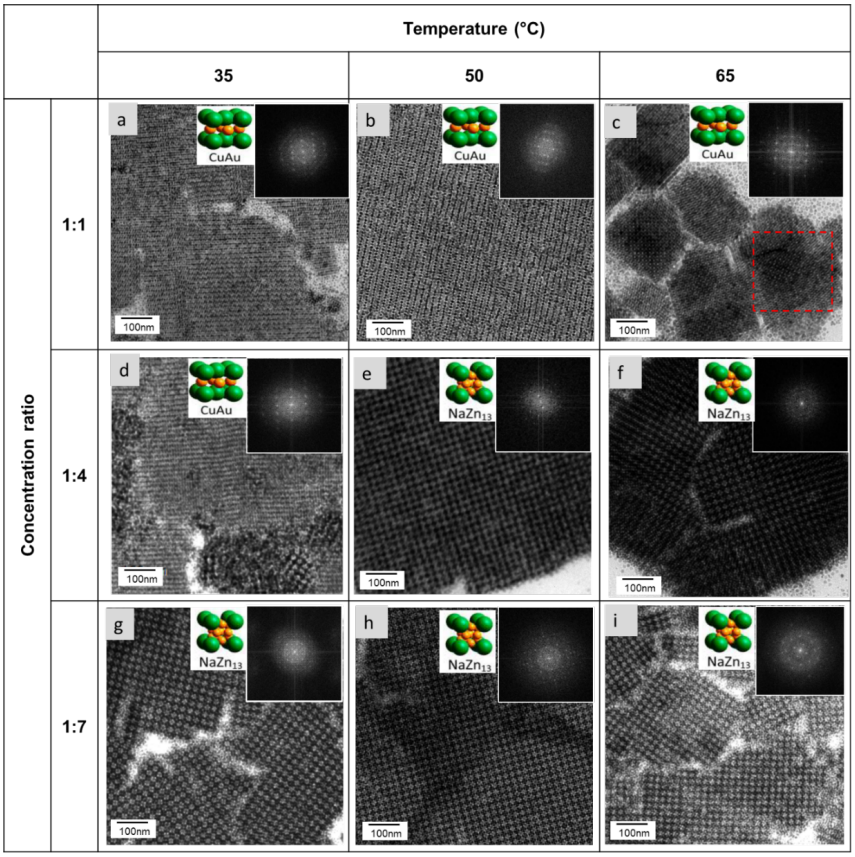

Figure 2. TEM images of binary superlattices formed with 7.9nm γ-Fe_2O_3 NPs and 4.6nm Au NPs at fixed effective size ratio (γ_{eff} =0.64), with various [γ-Fe_2O_3]/[Au] concentration ratios:1, 1:4 and 1:7, and various deposition temperatures: 35 °C, 50°C and 65 °C. Insets (right) show selected area FFT analysis. Insets (left) show unit cell of each BNSL structure corresponding to TEM image.

Table 4. Summary of the different crystal structures obtained according to the experimental conditions.

<table>
<tr><th>[γ-Fe2O3]/[Au]</th><th>γ_{eff}</th><th>T(°C)</th><th>BNSL structure</th></tr>
<tr><td rowspan="3">1/1</td><td rowspan="3">0.64</td><td>35</td><td rowspan="5">CuAu</td></tr>
<tr><td>50</td></tr>
<tr><td>65</td></tr>
<tr><td rowspan="3">1/4</td><td>0.64</td><td>35</td><td>CuAu & Amorphous</td></tr>
<tr><td>0.45</td><td rowspan="2">50</td><td>NaCl</td></tr>
<tr><td>0.64</td><td>65</td><td rowspan="2">$NaZn_{13}$</td></tr>
<tr><td>1/7</td><td>0.64</td><td>35</td></tr>
<tr><td>1/4</td><td>0.48</td><td>50</td><td>AlB_2</td></tr>
</table>

1.3. Effect of the solvent

At this point, we wonder if the final binary structure is solvent-dependent. So, we performed the deposition with γ-Fe_2O_3 NPs with 12.4 or 11.4 nm diameter and Au NPs with 4.6 nm, giving

effective size ratios γ_{eff} =0.45 or 0.48 (see Table 1), respectively. The deposition temperature is fixed at 50°C. Toluene and hexane are chosen as the solvents because of their quite different boiling point (111°C and 68°C respectively) leading to very different evaporation times (see Table S1 in SI). NaCl and AlB_2 type binary structures are observed for both solvents for γ_{eff}=0.45 and 0.48 respectively, in agreement with the well-known hard sphere model (see Table 3 and Figure 3). This result indicates that, in our conditions, the structure type of the BNSL does not depend on the evaporation kinetics i.e. the boiling point of the solvent.

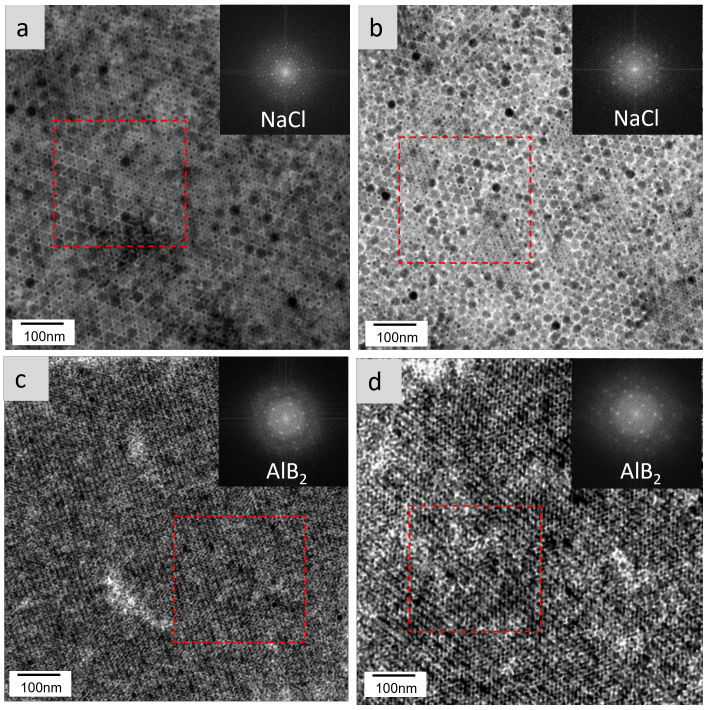

Figure 3 TEM images of binary superlattices composed of γ-Fe_2O_3 and Au NPs, with two effective size ratios, yeff = 0.45 (a and b) and 0.48 (c and d) and two solvents, toluene (a and c) and hexane (b and d). Insets show selected area FFT analysis for corresponding TEM images. Insets (left side from FFT diagram, (a and c)) show unit cell of each BNSL structure.

Nevertheless, depending on their chemical nature, solvents can interact differently with the ligand layer surrounding the NPs and thus alter the interparticle potential between NPs[33,36]. To study the evaporation kinetic effect on the BNSLs formation, we carried out BNSLs assembly

in aromatic solvent such as cumene to compare the resulting BNSLs with the ones obtained with toluene. These two solvents are characterized by similar dielectric and Hamaker constants (Table S1 Supporting Information) but quite different boiling points (T_b= 152 and 111°C respectively). The deposition is performed with γ-Fe_2O_3 NPs (7.9 nm) and Au NPs (4.6 nm) giving an effective size ratio γ_{eff} equal to 0.64 (table 1), the concentration ratio [γ-Fe_2O_3]/[Au] =1/4 and the deposition temperature T_d=50°C. TEM study evidences the formation of $NaZn_{13}$ type structure for BNSLs formed with both solvents, in agreement with the hard sphere model (Figure S5, Supporting Information). This result clearly confirms that the structure of the BNSL is independent of the evaporation kinetics, which indicates that the assembly process occurs mostly under thermodynamic control.

1.3.1. Effect of the deposition substrate

After focusing on the effects of the γ-Fe_2O_3/Au effective size ratio, the [γ-Fe_2O_3]/[Au] concentration ratio, the deposition temperature (T_d) and the nature of the solvent on the formation of BNSLs, we now focus on a last parameter: the substrate. In the case of heterogeneous growth, the substrate can play an important role on the superlattice growth. For example, in the case of mono-component superlattices, the coherence length of the organization depends on the substrate roughness as well as the interactions substrate-coated NPs[37]. In order to assess the effect of the substrate, we studied the BNSLs formation in the absence of solid substrate, what is possible by using the *liquid-liquid interface* deposition method[4,36]. This method is based on self-assemblies via two immiscible solvents. It is particularly interested to get rid of any substrate restrictions as the resulting film formed at the liquid surface can be easily transfer to any substrate. This study is performed with γ-Fe_2O_3 NPs (7.9 nm) and Au NPs (4.6 nm) given an effective size ratio, γ_{eff} equal to 0.64, two different concentration ratio 1/1

and 1/4, a deposition temperature, T_d equal to 50°C and toluene as the solvent. TEM study (Figures 4a and b) reveals the formation of similar type structures of BNSL domains as those observed by using the immersion method, i.e., CuAu and $NaZn_{13}$ for [γ–Fe_2O_3]/[Au] concentration ratio equal to 1/1 and 1/4 respectively (Figure 2). Nevertheless, the BNSLs appear clearly thicker and more widespread by using immersion method compared to the interface deposition. This result allows to conclude to the absence of impact of the substrate on the final BNSL type-structure.

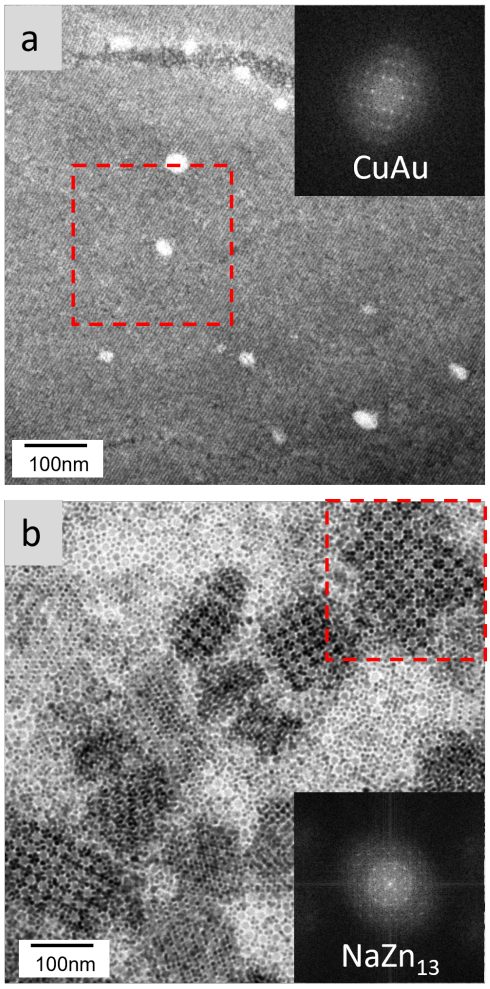

Figure 4. TEM images of binary superlattices formed with 7.9nm γ-Fe_2O_3 and 4.6nm Au NPs with fixed effective size ratio (γ_{eff} =0.64), at a fixed deposition temperature T_d=50°C by liquid-liquid interface method and at different concentration ration a) 1/1 and b) 1/4. Insets (right) show selected area FFT analysis. Insets (left) show unit cell of each BNSL structure corresponding to TEM image.

2- Effect of the insertion of Au NPs in mono-component superlattices of γ-Fe_2O_3 NPs on the magnetic properties

In order to study the effect of the presence of Au NPs in the superlattices of γ-Fe_2O_3 NPs on the magnetic properties, a comparative study at low field and high field have been performed involving i) the thin $NaZn_{13}$ binary superlattices composed of γ-Fe_2O_3 and Au NPs and ii) the thin superlattices composed of γ-Fe_2O_3 NPs. The measurements have been performed on the samples deposited on a TEM grid by using a SQUID magnetometer.

The $NaZn_{13}$ BNSLs (Figure S6) composed of few layers (3-4) are obtained with oleic acid coated γ-Fe_2O_3 NPs (7.9 nm) and dodecanethiol coated Au NPs (4.6 nm). The deposition conditions are listed in Table 2. Mono-component superlattices composed of γ-Fe_2O_3 NPs are obtained by using the same synthetic batch of oleic acid coated γ-Fe_2O_3 NPs (7.9 nm) and same solvent (toluene) used to form the corresponding BNSLs (Figure S6a, Supporting Information).

A prerequisite to this comparative magnetic study is the determination of the core-to-core interparticle distances $D_{c\text{-}c}$ between maghemite NPs in both types of assemblies, which has been made by TEM study. While TEM image obtained at low magnification, confirms the cubic lattices of BNSLs (Figure S7a, Supporting Information), higher magnification images (Figure S7b and S7c, Supporting Information) allow to distinguish the γ-Fe_2O_3 (light grey) and the Au (black) NPs since gold atoms scatter electrons more strongly than iron oxide. From the contrast profile made over the red line, one can deduce the core-to-core interparticle distance $D_{c\text{-}c}$ between maghemite in BNSL (Figure S6 c and d, Supporting Information), which is found around 13.8 nm (Table S2). For pure γ-Fe_2O_3 superlattices, the TEM image illustrates the close packed arrangement of the magnetic NPs (Figure S6, Supporting Information). From the contrast profile performed along the red line of the TEM image, the core-to-core interparticle distance $D_{c\text{-}c}$ between maghemite is found around 10 nm (Table S2 and Figure S7b, Supporting

Information). From this $D_{c\text{-}c}$ value and maghemite NP size, we deduce an edge-to-edge distance around 2.1 nm, which indicates the absence of interdigitation between the oleic acid chains surrounding the NPs (effective length 1.1nm). This result is in agreement with previous results[32].

From this comparative structural study, we deduce that the pure maghemite NPs assemblies are distorted by the presence of gold, which induces an increase in distance $D_{c\text{-}c}$ between maghemite in the BNSLs. In light of this result, one can expect a change in the magnetic dipole-dipole interactions between maghemite NPs in the BNSLs.

Maghemite NPs with a mean diameter of 7.9 nm, are small enough to have a single magnetic domain. In that case, in an assembly of NPs, each nanoparticle acts like a giant or "superspin". In sufficiently concentrated systems as this is the case in superlattices, these superspins can interact via long-range dipolar interactions[38]. The magnetic measurements we performed, allow to learn about these dipolar interactions, which are, in light of the structural characterizations, expected to change between the two samples. Figure 5a shows the field-cooled (FC) and zero field cooled (ZFC) magnetization versus temperature curves for pure γ-Fe_2O_3 superlattices and $NaZn_{13}$ binary γ-Fe_2O_3-Au superlattices. In a general trend, as the sample has been cooled in zero field, there is no net alignment of the superspins (here at 3 K) and hence the magnetization is close to zero. A small magnetic field (20 Oe) is applied. As the temperature is increased, the superspins become progressively 'unblocked', aligning towards the field direction and the magnetization increases until it reaches a maximum which we define here as the blocking temperature, T_B. Above T_B the behavior is paramagnetic i.e. the thermal energy increases to such an extent that the increased dynamic rotation of the superspins prevents alignment in the field direction and the magnetization decreases with increasing temperature. In the FC curve, the magnetization is larger than that of the ZFC curve from 3K to T_B. Above T_B the behavior is paramagnetic, and the magnetization decreases with increasing temperature and join the ZFC

curve. The pure γ-Fe_2O_3 superlattices are characterized by a T_B of around 84 K (Table S3, Supporting Information). This value is in good agreement with the values reported in the literature for the same size of NPs[32]. The blocking temperature accounts of the energy barriers of the magnetic nanoparticles (E_b), which depend on both the anisotropy energy (size, nanocrystallinity and shape) $E_a = k_a V$ and the dipole interaction energy, E_{dd}. The narrowness of the ZFC peak indicates here, a narrow distribution of energy barriers, that is to say a low size distribution of the maghemite NCs in the sample. The low slope of the FC curve, at low temperature, is indicative of rather strong dipolar interactions between the nanoparticles. For the binary superlattices, we observe a significant decrease in the T_B from 84 K to 76 K (Table S3, Supporting Information). As the two samples are made with the same batch of γ-Fe_2O_3 NPs, this change in T_B cannot result from a change in anisotropy or size of the nanoparticles. The T_B decrease is explained by the decrease in the dipolar interactions between the γ-Fe_2O_3 NPs, resulting from the increase in the core-to-core interparticle distance $D_{c\text{-}c}$ distance (from 10 nm to 13.8 nm) between magnetic NPs in the binary superlattices compared to the pure maghemite superlattices[32,39]. Such a drop in T_B of 8 K, i.e of 10%, is in good agreement with what has been observed for binary superlattices made of polyoxometalates and maghemite nanocrystals[32] and attributed to a decrease in the dipole-dipole-interaction arising from an increase in the core-to-core interparticle distance[40]. Besides, we see that there is a slight increase of the slope in the field cooled magnetization curve with temperature below T_B for the BNSLs compared to the pure maghemite superlattices. As previously, this feature is explained by the decrease in the NP dipolar interaction in the assembly, and well agrees with the T_B decrease.

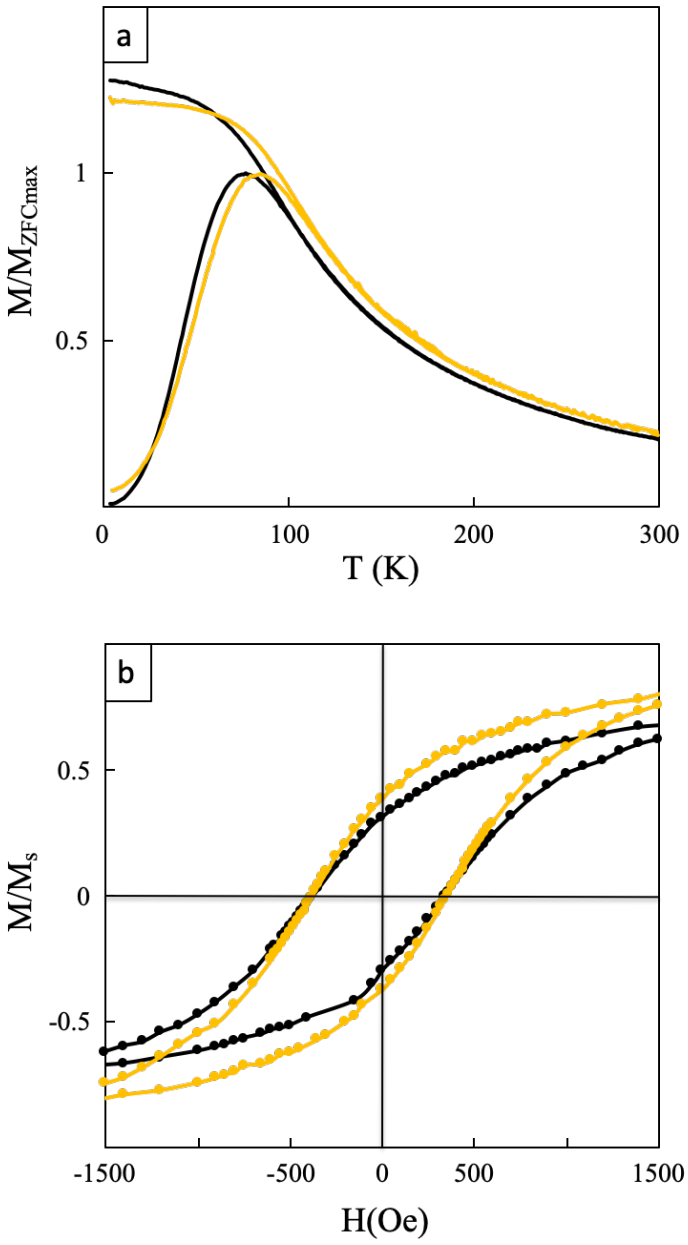

Figure 5. SQUID measurements in thin layers of $NaZn_{13}$ binary structure composed of 7.9 nm γ-Fe_2O_3 and 4.6 nm Au NPs (black curve) and for a pure 7.9 nm γ-Fe_2O_3 NPs (orange curve). (a) Temperature dependence of the magnetization in the zero-field cooled/field cooled (ZFC/FC) with in-plane field of 20 Oe and (b) hysteresis curves performed at 3K.

Figure 5b shows the magnetization as a function of field for pure γ-Fe_2O_3 superlattices and $NaZn_{13}$ binary γ-Fe_2O_3-Au superlattices. The measurements have been performed at 3 K. The

magnetic signatures (at high field) of both samples appear similar. Independently of the presence of Au NPs in the thin superlattices, the coercive field (H_c) is found equal to around 360 Oe (Table S3, Supporting Information). The change in the dipolar interaction, resulting in the change of T_B, is expected to also impact H_c. However, it is not the case. At this stage of the study, the invariance of H_c we observe, cannot be explained.

These results clearly evidence an effect of the insertion of Au NPs in the superlattices of γ-Fe_2O_3. As a result of an increase in the interparticle distance in the binary superlattices compared to the pure γ-Fe_2O_3 superlattices, we observe a decrease in the dipolar magnetic interactions between magnetic NPs. So, 4.6 nm Au NPs can be used as spacer between 7.9nm γ-Fe_2O_3 NPs in binary assemblies to tune the dipole interactions between γ-Fe_2O_3 NPs.

CONCLUSION

In conclusion, we have shown that designing different crystalline structures of binary superlattices by mixing γ-Fe_2O_3 and Au NPs, is possible. One of the key factors to control BNSL structure is the effective size ratio. By increasing the effective size ratio, the BNSL type-structure changes from NaCl to AlB_2 and $NaZn_{13}$ in accordance with the phase diagram for binary hard spheres mixtures. The effects of concentration ratio ([γ-Fe_2O_3]/[Au]) and deposition temperature were also investigated. It is shown that they can influence the final structure of the binary superlattice, alone or combined with each other. Moreover, the final BNSL structure is non-solvent dependent i.e. it does not depend on the evaporation kinetics. This result shows that the assembly process takes place mainly under thermodynamic control. The magnetic properties were investigated on thin Au NPs / γ-Fe_2O_3 NPs binary and pure γ-Fe_2O_3 NPs SLs using SQUID magnetometry. We clearly evidenced an effect of the insertion of Au NPs in the superlattices of γ-Fe_2O_3. As a result of an increase in the interparticle distance in the binary

superlattices compared to the pure γ-Fe_2O_3 superlattices, we observe a decrease in the dipolar magnetic interactions between magnetic NPs.

Our findings are of particular importance for the design of novel 3D functional materials and could be extended to other couple of NPs with different properties (plasmonic/plasmonic or plasmonic/magnetic or plasmonic/catalytic) to get optimal coupling and enhance synergistic effect between binary component for magnetic, plasmonic or catalytic applications.

■ ASSOCIATED CONTENT

Supporting Information

TEM images of the γ-Fe_2O_3 and Au nanoparticles used to produce the binary superlattices. Scheme illustrated the preparation method used for growing binary superlattices. Hildebrand parameters of the different solvents studied, structural characteristics of binary superlattices, TEM images of binary superlattices with various crystal planes and data relevant for SQUID measurements. This material is available free of charge via the Internet at http://pubs.acs.org

■ AUTHOR INFORMATION

Corresponding authors

*E-mail 1 : alexa.courty@sorbonne-universite.fr

* E-mail 2 : isabelle.lisiecki@sorbonne-universite.fr

Author contributions

The manuscript was written through contributions of all authors. All authors have given approval to the final version of the manuscript.

■ **ACKNOWLEDGMENTS**

The authors thank Dr David Hrabosky for fruitful discussions and the staff of the MPBT (physical properties – low temperature) platform of Sorbonne University for their support in SQUID measurements.

■ **REFERENCES**

(1) Su, B.; Guo, W.; Jiang, L. Learning from Nature: Binary Cooperative Complementary Nanomaterials. *Small* **2015**, *11* (9–10), 1072–1096. https://doi.org/10.1002/smll.201401307.

(2) Brune, H.; Courty, A.; Petit, C.; Repain, V. *Self-Assembly of Nanoalloys, Nanoalloys for Fundamental Energy to Application*, Florent Calvo.; 2013.

(3) Boles, M. A.; Engel, M.; Talapin, D. V. Self-Assembly of Colloidal Nanocrystals: From Intricate Structures to Functional Materials. *Chem. Rev.* **2016**, *116* (18), 11220–11289. https://doi.org/10.1021/acs.chemrev.6b00196.

(4) Shevchenko, E. V.; Talapin, D. V.; Murray, C. B.; O'Brien, S. Structural Characterization of Self-Assembled Multifunctional Binary Nanoparticle Superlattices. *J. Am. Chem. Soc.* **2006**, *128* (11), 3620–3637. https://doi.org/10.1021/ja0564261.

(5) Boles, M. A.; Talapin, D. V. Many-Body Effects in Nanocrystal Superlattices: Departure from Sphere Packing Explains Stability of Binary Phases. *J. Am. Chem. Soc.* **2015**, *137* (13), 4494–4502. https://doi.org/10.1021/jacs.5b00839.

(6) Henry, A.-I.; Courty, A.; Pileni, M.-P.; Albouy, P.-A.; Israelachvili, J. Tuning of Solid Phase in Supracrystals Made of Silver Nanocrystals. *Nano Lett.* **2008**, *8* (7), 2000–2005.

(7) Ouhenia-Ouadahi, K.; Andrieux-Ledier, A.; Richardi, J.; Albouy, P.-A.; Beaunier, P.; Sutter, P.; Sutter, E.; Courty, A. Tuning the Growth Mode of 3D Silver Nanocrystal Superlattices by Triphenylphosphine. *Chem. Mater.* **2016**, *28* (12), 4380–4389. https://doi.org/10.1021/acs.chemmater.6b01374.

(8) Pileni, M. P. Nanocrystal Self-Assemblies: Fabrication and Collective Properties. *J. Phys. Chem. B* **2001**, *105* (17), 3358–3371. https://doi.org/10.1021/jp0039520.

(9) Si, K. J.; Chen, Y.; Shi, Q.; Cheng, W. Nanoparticle Superlattices: The Roles of Soft Ligands. *Adv. Sci.* **2018**, *5* (1), 1700179. https://doi.org/10.1002/advs.201700179.

(10) Courty, A.; Richardi, J.; Albouy, P.-A.; Pileni, M.-P. How To Control the Crystalline Structure of Supracrystals of 5-Nm Silver Nanocrystals. *Chem. Mater.* **2011**, *23* (18), 4186–4192. https://doi.org/10.1021/cm201313r.

(11) Parker, D.; Lisiecki, I.; Salzemann, C.; Pileni, M.-P. Emergence of New Collective Properties of Cobalt Nanocrystals Ordered in Fcc Supracrystals: II, Magnetic Investigation. *J. Phys. Chem. C* **2007**, *111* (34), 12632–12638. https://doi.org/10.1021/jp071821u.

(12) Goubet, N.; Richardi, J.; Albouy, P. A.; Pileni, M. P. How to Predict the Growth Mechanism of Supracrystals from Gold Nanocrystals. *J. Phys. Chem. Lett.* **2011**, *2* (5), 417–422. https://doi.org/10.1021/jz200004f.

(13) Murray, M. J.; Sanders, J. V. Close-Packed Structures of Spheres of Two Different Sizes II. The Packing Densities of Likely Arrangements. *Philos. Mag. A* **1980**, *42* (6), 721–740. https://doi.org/10.1080/01418618008239380.

(14) Evers, W. H.; Nijs, B. D.; Filion, L.; Castillo, S.; Dijkstra, M.; Vanmaekelbergh, D. Entropy-Driven Formation of Binary Semiconductor-Nanocrystal Superlattices. *Nano Lett.* **2010**, *10* (10), 4235–4241. https://doi.org/10.1021/nl102705p.

(15) Yang, Z.; Wei, J.; Pileni, M.-P. Metal–Metal Binary Nanoparticle Superlattices: A Case Study of Mixing Co and Ag Nanoparticles. *Chem. Mater.* **2015**, *27* (6), 2152–2157. https://doi.org/10.1021/acs.chemmater.5b00123.

(16) Chen, J.; Dong, A.; Cai, J.; Ye, X.; Kang, Y.; Kikkawa, J. M.; Murray, C. B. Collective Dipolar Interactions in Self-Assembled Magnetic Binary Nanocrystal Superlattice Membranes. *Nano Lett.* **2010**, *10* (12), 5103–5108. https://doi.org/10.1021/nl103568q.

(17) Wang, K.; Li, F.; Jin, S.-M.; Wang, K.; Tian, D.; Hussain, M.; Xu, J.; Zhang, L.; Liao, Y.; Lee, E.; Yi, G.-R.; Xie, X.; Zhu, J. Chain-Length Effect on Binary Superlattices of Polymer-Tethered Nanoparticles. *Mater. Chem. Front.* **2020**, *4* (7), 2089–2095. https://doi.org/10.1039/D0QM00194E.

(18) Kiely, C. J.; Fink, J.; Brust, M.; Bethell, D.; Schiffrin, D. J. Spontaneous Ordering of Bimodal Ensembles of Nanoscopic Gold Clusters. *Nature* **1998**, *396* (6710), 444–446. https://doi.org/10.1038/24808.

(19) Shevchenko, E. V.; Ringler, M.; Schwemer, A.; Talapin, D. V.; Klar, T. A.; Rogach, A. L.; Feldmann, J.; Alivisatos, A. P. Self-Assembled Binary Superlattices of CdSe and Au

Nanocrystals and Their Fluorescence Properties. *J. Am. Chem. Soc.* **2008**, *130* (11), 3274–3275. https://doi.org/10.1021/ja710619s.

(20) Brittman, S.; Mahadik, N. A.; Qadri, S. B.; Yee, P. Y.; Tischler, J. G.; Boercker, J. E. Binary Superlattices of Infrared Plasmonic and Excitonic Nanocrystals. *ACS Appl. Mater. Interfaces* **2020**, *12* (21), 24271–24280. https://doi.org/10.1021/acsami.0c03805.

(21) Sánchez, E. H.; Vasilakaki, M.; Lee, S. S.; Normile, P. S.; Muscas, G.; Murgia, M.; Andersson, M. S.; Singh, G.; Mathieu, R.; Nordblad, P.; Ricci, P. C.; Peddis, D.; Trohidou, K. N.; Nogués, J.; De Toro, J. A. Simultaneous Individual and Dipolar Collective Properties in Binary Assemblies of Magnetic Nanoparticles. *Chem. Mater.* **2020**, *32* (3), 969–981. https://doi.org/10.1021/acs.chemmater.9b03268.

(22) Zheng, N.; Fan, J.; Stucky, G. D. One-Step One-Phase Synthesis of Monodisperse Noble-Metallic Nanoparticles and Their Colloidal Crystals. *J. Am. Chem. Soc.* **2006**, *128* (20), 6550–6551. https://doi.org/10.1021/ja0604717.

(23) Andrieux-Ledier, A.; Tremblay, B.; Courty, A. Stability of Self-Ordered Thiol-Coated Silver Nanoparticles: Oxidative Environment Effects. *Langmuir* **2013**, *29* (43), 13140–13145. https://doi.org/10.1021/la402916b.

(24) Ngo, A.-T.; Richardi, J.; Pileni, M. P. Crack Patterns in Superlattices Made of Maghemite Nanocrystals. *Phys. Chem. Chem. Phys.* **2013**, *15* (26), 10666. https://doi.org/10.1039/c3cp50276g.

(25) Park, J.; An, K.; Hwang, Y.; Park, J.-G.; Noh, H.-J.; Kim, J.-Y.; Park, J.-H.; Hwang, N.-M.; Hyeon, T. Ultra-Large-Scale Syntheses of Monodisperse Nanocrystals. *Nat. Mater.* **2004**, *3* (12), 891–895. https://doi.org/10.1038/nmat1251.

(26) Courty, A. Silver Nanocrystals: Self-Organization and Collective Properties. *J. Phys. Chem. C* **2010**, *114* (9), 3719–3731. https://doi.org/10.1021/jp908966b.

(27) Yang, Z.; Altantzis, T.; Bals, S.; Tendeloo, G. V.; Pileni, M.-P. Do Binary Supracrystals Enhance the Crystal Stability? *J. Phys. Chem. C* **2018**, *122* (25), 13515–13521. https://doi.org/10.1021/acs.jpcc.7b12373.

(28) Dong, A.; Chen, J.; Vora, P. M.; Kikkawa, J. M.; Murray, C. B. Binary Nanocrystal Superlattice Membranes Self-Assembled at the Liquid–Air Interface. *Nature* **2010**, *466* (7305), 474–477. https://doi.org/10.1038/nature09188.

(29) Wu, Y.; Li, S.; Gogotsi, N.; Zhao, T.; Fleury, B.; Kagan, C. R.; Murray, C. B.; Baxter, J. B. Directional Carrier Transfer in Strongly Coupled Binary Nanocrystal Superlattice Films Formed by Assembly and in Situ Ligand Exchange at a Liquid–Air Interface. *J. Phys. Chem. C* **2017**, *121* (8), 4146–4157. https://doi.org/10.1021/acs.jpcc.6b12327.

(30) Eldridge, M. D.; Madden, P. A.; Frenkel, D. Entropy-Driven Formation of a Superlattice in a Hard-Sphere Binary Mixture. *Nature* **1993**, *365* (6441), 35–37. https://doi.org/10.1038/365035a0.

(31) Wei, J.; Schaeffer, N.; Pileni, M.-P. Ligand Exchange Governs the Crystal Structures in Binary Nanocrystal Superlattices. *J. Am. Chem. Soc.* **2015**, *137* (46), 14773–14784. https://doi.org/10.1021/jacs.5b09959.

(32) Breitwieser Romain; Auvray Thomas; Volatron Florence; Salzemann Caroline; Ngo Anh-Tu; Albouy Pierre-Antoine; Proust Anna; Petit Christophe. Binary Superlattices from {Mo132} Polyoxometalates and Maghemite Nanocrystals: Long-Range Ordering and Fine-Tuning of Dipole Interactions. *Small* **2016**, *12* (2), 220–228. https://doi.org/10.1002/smll.201502127.

(33) Evers, W. H.; Nijs, B. D.; Filion, L.; Castillo, S.; Dijkstra, M.; Vanmaekelbergh, D. Entropy-Driven Formation of Binary Semiconductor-Nanocrystal Superlattices. *Nano Lett.* **2010**, *10* (10), 4235–4241. https://doi.org/10.1021/nl102705p.

(34) Filion, L.; Dijkstra, M. Prediction of Binary Hard-Sphere Crystal Structures. *Phys. Rev. E* **2009**, *79* (4), 046714. https://doi.org/10.1103/PhysRevE.79.046714.

(35) Ye, X.; Zhu, C.; Ercius, P.; Raja, S. N.; He, B.; Jones, M. R.; Hauwiller, M. R.; Liu, Y.; Xu, T.; Alivisatos, A. P. Structural Diversity in Binary Superlattices Self-Assembled from Polymer-Grafted Nanocrystals. *Nat. Commun.* **2015**, *6* (1), 10052. https://doi.org/10.1038/ncomms10052.

(36) Bodnarchuk, M. I.; Kovalenko, M. V.; Heiss, W.; Talapin, D. V. Energetic and Entropic Contributions to Self-Assembly of Binary Nanocrystal Superlattices: Temperature as the Structure-Directing Factor. *J. Am. Chem. Soc.* **2010**, *132* (34), 11967–11977. https://doi.org/10.1021/ja103083q.

(37) Laurence Motte, Alexa Courty, Anh-Tu Ngo, Isabelle Lisiecki, Marie-Paule Pileni. Self-Organization of Inorganic Nanocrystals. In *Nanocrystals Forming Mesoscopic Structures*; Wiley-VCH Verlag GmbH & Co. KGaA, 2005; pp 1–47.

(38) Parker, D.; Lisiecki, I.; Pileni, M. P. Do 8 Nm Co Nanocrystals in Long-Range-Ordered Face-Centered Cubic (Fcc) Supracrystals Show Superspin Glass Behavior? *J. Phys. Chem. Lett.* **2010**, *1* (7), 1139–1142. https://doi.org/10.1021/jz1001874.

(39) Costanzo, S.; Ngo, A. T.; Russier, V.; Albouy, P. A.; Simon, G.; Colomban, Ph.; Salzemann, C.; Richardi, J.; Lisiecki, I. Enhanced Structural and Magnetic Properties of Fcc Colloidal Crystals of Cobalt Nanoparticles. *Nanoscale* **2020**, *12* (47), 24020–24029. https://doi.org/10.1039/D0NR05517D.

(40) Bae, C. J.; Angappane, S.; Park, J.-G.; Lee, Y.; Lee, J.; An, K.; Hyeon, T. Experimental Studies of Strong Dipolar Interparticle Interaction in Monodisperse Fe3O4 Nanoparticles. *Appl. Phys. Lett.* **2007**, *91* (10), 102502. https://doi.org/10.1063/1.2778758.

Structural diversity in binary superlattices from Au and γ-Fe_2O_3 nanocrystals: towards fine tuning of dipolar interactions

Suyeon Lee[1], Anh-Tu Ngo[1], Isabelle Lisiecki[1]* and Alexa Courty[1]*

1-Sorbonne Université, MONARIS, UMR8233, UMR 8233, F-75005 Paris, France

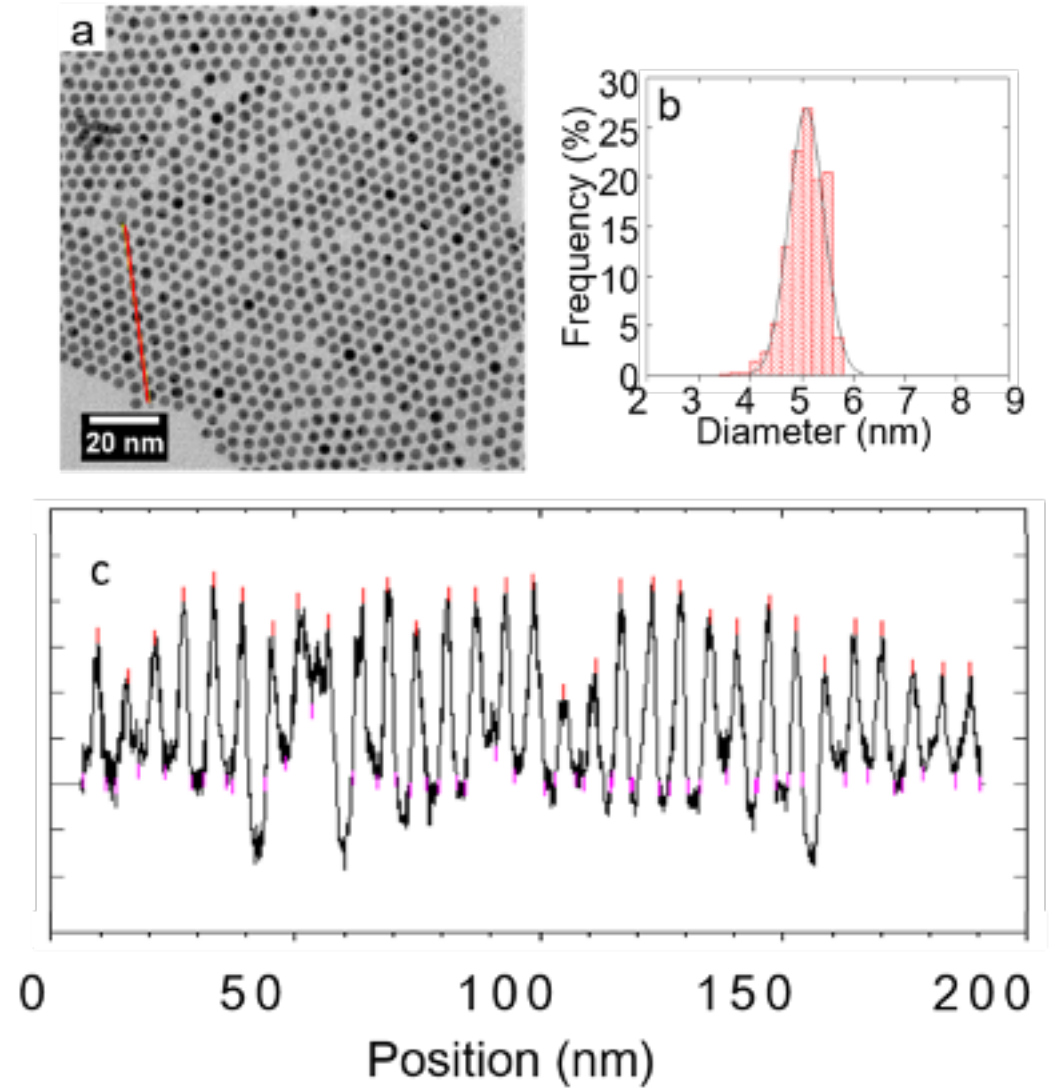

Figure S1. a) TEM image of 4.6 ± 0.3 nm Au NPs , b) corresponding size distribution and c) contrast profile made over the red line allowing to determine the effective diameter $D_{C\text{-}C}$*≈6.4 nm.*

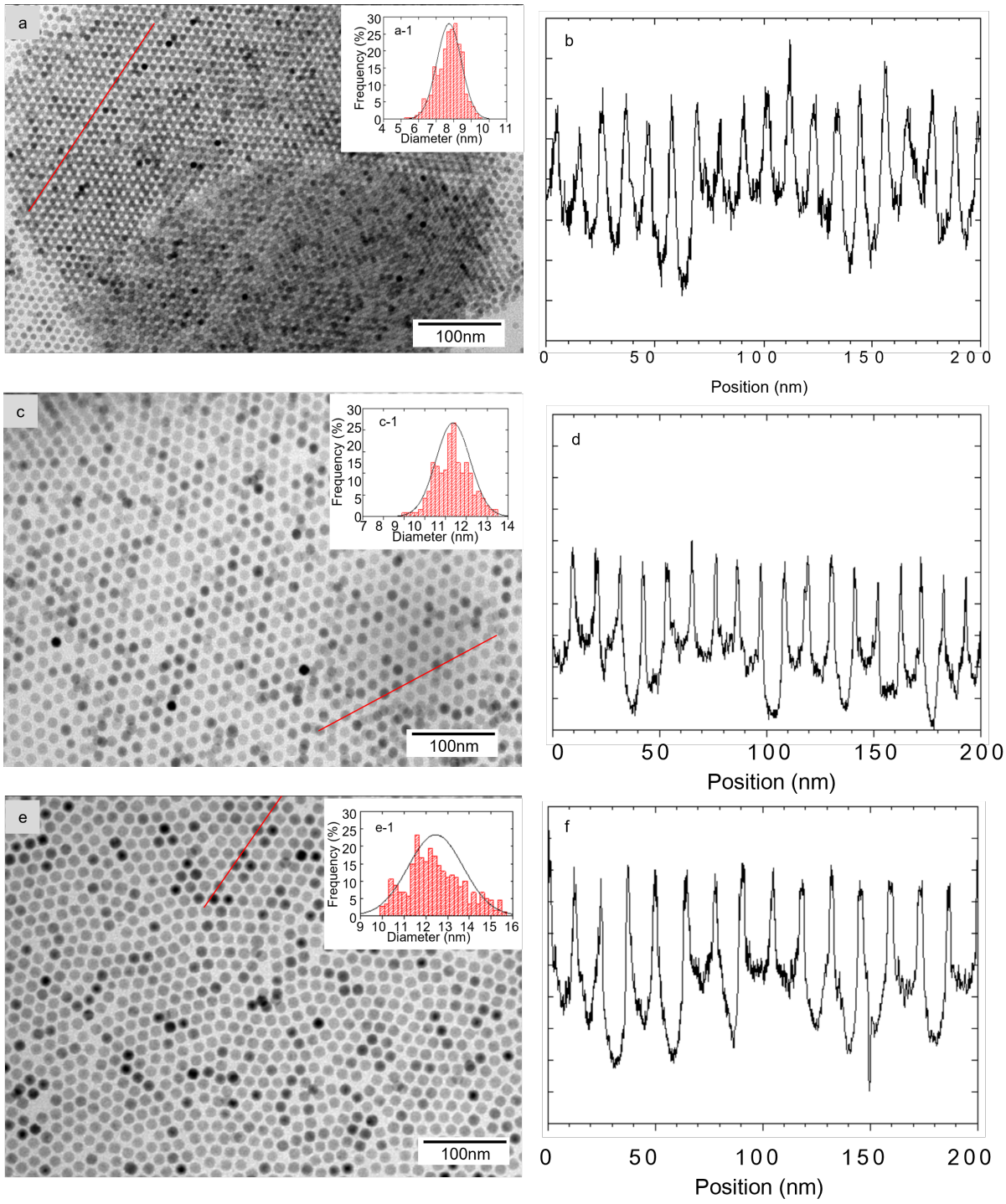

Figure S2. TEM images of γ-Fe_2O_3 NPs of different diameters and contrast profiles made over the red lines, allowing the determination of corresponding effective diameters $D_{C\text{-}C}$ *: a) D=7.9 ±0.6 nm b)* $D_{c\text{-}c}$ *≈ 10nm c) D=11.4±0.9 nm d)* $D_{c\text{-}c}$ *≈ 13.4 nm e) D=12.4±1.0 nm f)* $D_{c\text{-}c}$ *≈14.2nm.*

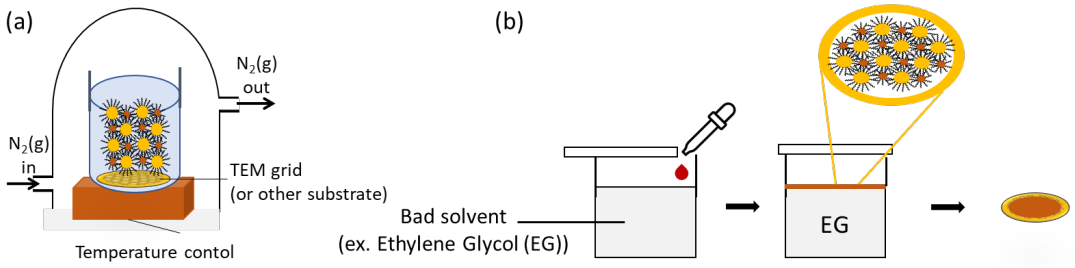

Figure S3: Schemes of preparation methods used for growing ordered binary superlattices.

Table S1 Hildebrand parameters and boiling points of the different solvents used in this study[29–31].

Solvent or (ligands)	Hildebrand solubility parameters ($MPa^{0.5}$)	Dielectric constant	Boiling point (°C)	Evaporation time (hour)
Toluene	18.2	2.38	111	4
Cumene	17.5	2.4	152	5
Hexane	14.9	1.8	68	0.5

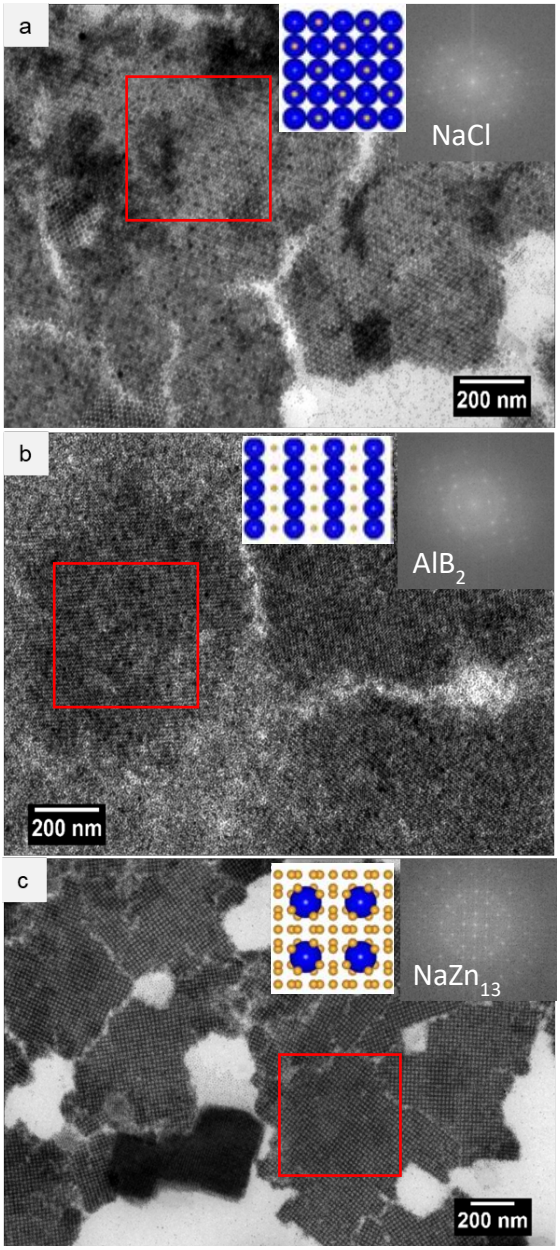

Figure S4. TEM images of BNSLs composed of γ-Fe_2O_3 and Au NPs, with different effective size ratios (γ_{eff}), keeping the other conditions unchanged ([γ-Fe_2O_3]/[Au])=1/4, T_d=50°C), γ_{eff} = (a) 0.45 (b) 0.48 (c) 0.64. Insets: the FFT analysis performed on selected areas (red squares) of the binary superlattices and BNSL structures corresponding to TEM images.

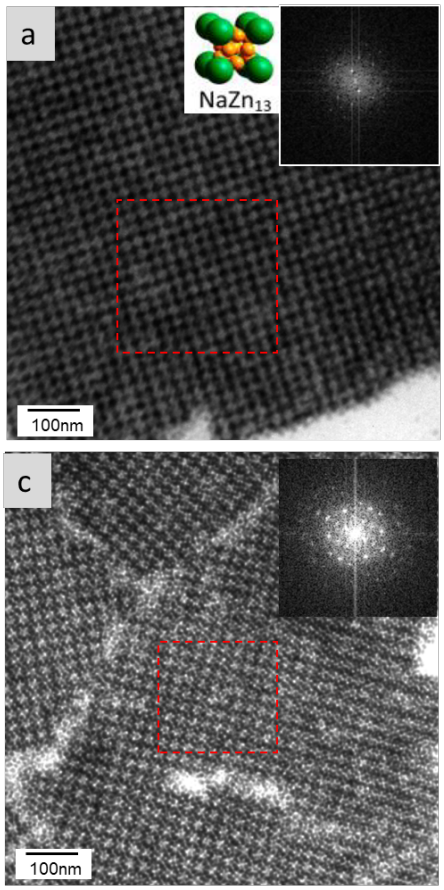

Figure S5. TEM images of $NaZn_{13}$ type binary superlattices formed with 7.9nm γ-Fe_2O_3 and 4.6nm Au NPs with fixed effective size ratio (γ_{eff} =0.64) and deposition temperature Td=50°C by using different solvents a) toluene and b) cumene. Insets: the FFT analysis performed on selected areas (red squares) of the binary superlattices and representation of unit cell of $NaZn_{13}$ type binary structure.

Table S2. Interparticle distance $D_{C\text{-}C}$ between magnetic NPs (γ-Fe_2O_3 NPs) in thin BNSLs and pure γ-Fe_2O_3 NP assemblies.

	Binary superlattices formed with 7.9 nm γ-Fe_2O_3 and 4.6 nm Au NPs	**Pure 7.9 nm γ-Fe_2O_3 NP superlattices**
$D_{C\text{-}C}$	13.8 nm	10 nm
Crystalline structure	$NaZn_{13}$	*fcc*

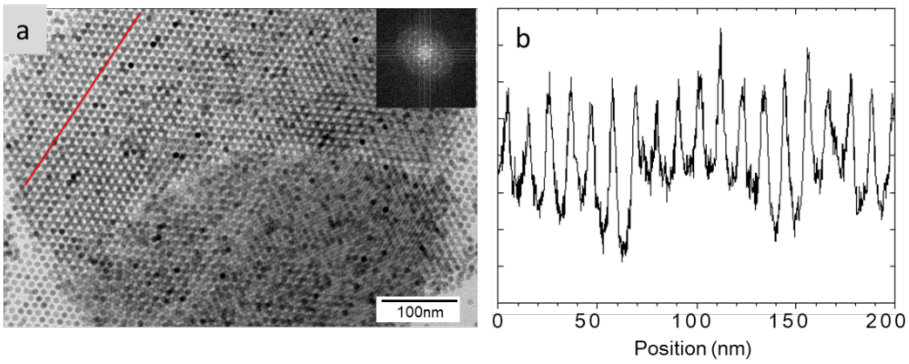

Figure S6. (a) TEM image of thin layers of γ-Fe_2O_3 NPs with their FFT image (inset) and (b) the contrast profile made over the red line, indicating an interparticle distances $D_{C\text{-}C}\approx 10$ nm.

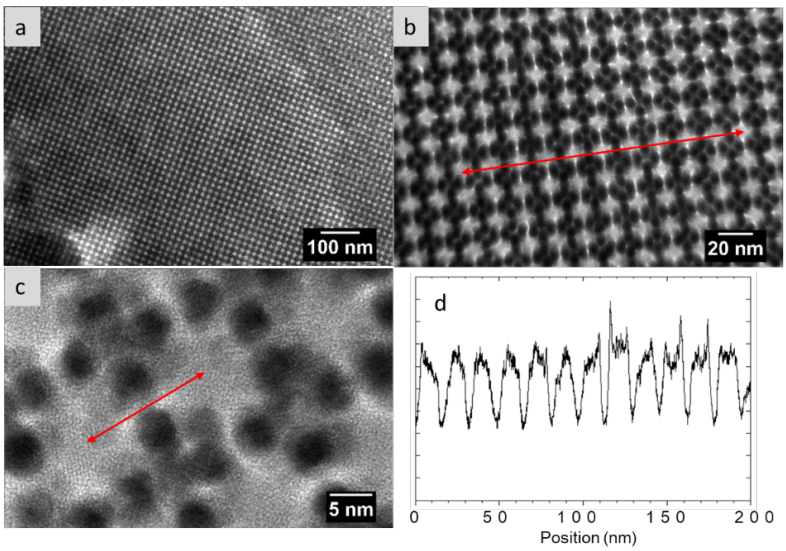

Figure S7. (a-c) HR-TEM images of $NaZn_{13}$ BNSL structure at different magnifications and (d) the contrast profile made over the red line, from (b) indicating an interparticle distances $D_{C-C} \approx 13.8$ nm.

Table S3. Comparison of the blocking temperature and the coercivity values obtained by SQUID measurements for pure γ-Fe_2O_3 superlattices and γ-Fe_2O_3 -Au BNSLs. All values are deduced from Figure 6.

	SQUID	
	Blocking temperature, T_b (K)	**Coercivity, H_c (Oe)**
γ-Fe_2O_3 superlattices	84	360
γ-Fe_2O_3-Au BNSLs	76	360